

Properties of Contact and Bulk Impedances in Hybrid Lead Halide Perovskite Solar Cells Including Inductive Loop Elements

Antonio Guerrero,^{*,†} Germà Garcia-Belmonte,[†] Ivan Mora-Sero,[†] Juan Bisquert,^{*,†,‡} Yong Soo Kang,[§] T. Jesper Jacobsson,^{||} Juan-Pablo Correa-Baena,^{||} and Anders Hagfeldt^{*,‡,||}

[†]Institute of Advanced Materials (INAM), Universitat Jaume I, 12006 Castelló, Spain

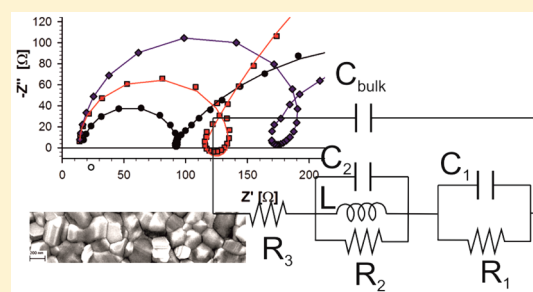
[‡]Department of Chemistry, Faculty of Science, King Abdulaziz University, Jeddah 21589, Saudi Arabia

[§]Center for Next Generation Dye-sensitized Solar Cells, Department of Energy Engineering, Hanyang University, 133-791, Seoul, Republic of Korea

^{||}Laboratory for Photomolecular Science, Institute of Chemical Sciences and Engineering, École Polytechnique Fédérale de Lausanne, CH-1015-Lausanne, Switzerland

Supporting Information

ABSTRACT: Impedance spectroscopy offers access to all the different electronic and ionic processes taking place simultaneously in an operating solar cell. To date, its use on perovskite solar cells has been challenging because of the richness of the physical processes occurring within similar time domains. The aim of this work is to understand the general impedance response and propose a general equivalent circuit model that accounts for the different processes and gives access to quantitative analysis. When the electron-selective contacts and the thickness of the perovskite film are systematically modified, it is possible to distinguish between the characteristic impedance signals of the perovskite layer and those arising from the contacts. The study is carried out using mixed organic lead halogen perovskite ($\text{FA}_{0.85}\text{MA}_{0.15}\text{Pb}(\text{I}_{0.85}\text{Br}_{0.15})_3$) solar cells with three different electron-selective contacts: SnO_2 , TiO_2 , and Nb_2O_5 . The contacts have been deposited by atomic layer deposition (ALD), which provides pinhole-free films and excellent thickness control in the absence of a mesoporous layer to simplify the impedance analysis. It was found that the interfacial impedance has a rich structure that reveals different capacitive processes, serial steps for electron extraction, and a prominent inductive loop related to negative capacitance at intermediate frequencies. Overall, the present report provides insights into the impedance response of perovskite solar cells which enable an understanding of the different electronic and ionic processes taking place during device operation.



INTRODUCTION

Perovskite materials have recently been used as light-harvesters in emerging photovoltaic technologies.^{1–3} Engineering of the active and extraction layers has resulted in impressive efficiencies as high as 20.8% in research articles,^{4–7} and the current certified record efficiency is 21.0% held by the Laboratory of Photomolecular Science and Laboratory of Photonics and Interfaces (EPFL) (certified by Newport Corporation in Bozeman, Montana). These recent developments demonstrate an enormous potential of perovskite solar cells, suggesting that they may soon compete with already commercially available photovoltaic technologies.

Interfacial layers have certainly proved to be key for the achievement of these high efficiencies, and further improvements are expected.⁵ However, there are many aspects related to the contacts which are still poorly understood. For example, it has been shown that polarization of the devices can switch completely the sense of the current flow.⁸ Recently, hysteresis on the current density–voltage (J – V) response has been explained by the presence of two contributions, both connected

with the extraction of carriers at the contacts, which take place at different time scales.⁹ While capacitive current is on the order of seconds, a slow redistribution of mobile ions requires several minutes. Indeed, the effect of ion migration toward the external electrodes has been reported to provide chemical reactions with the TiO_2 and Spiro-OMeTAD selective layers¹⁰ and can lead to the degradation of the interfaces with the contacts.¹¹ Therefore, detailed understanding on the interactions between perovskites and its contacts is still missing, and this topic requires further investigation.

Impedance spectroscopy has proved to be a useful tool for the investigations of different types of solar cells, such as the dye-sensitized solar cells, where the electronic and ionic processes are very well differentiated.¹² In impedance spectroscopy technique, a small ac perturbation (i.e. 20 mV) is applied to the working device using a wide range of frequencies

Received: February 19, 2016

Revised: March 31, 2016

Published: April 2, 2016



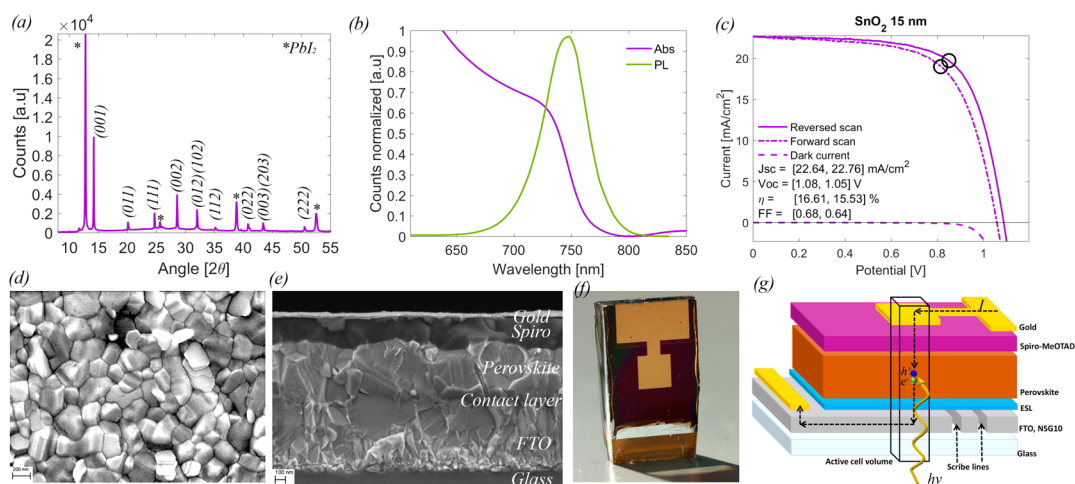


Figure 1. (a) XRD spectrum of the perovskite spin-coated onto a soda lime glass substrate. (b) Absorption and photoluminescence data. The data is normalized, and the data is background corrected. (c) J - V data for the best performing device investigated here. (d) Top view SEM image of a perovskite film. (e) Cross-section SEM image of a typical device. (f) Photo of a typical device. The width of the device is 1.4 cm. (g) An illustration of the cell architecture.

(megahertz to millihertz) and the differential current output is measured. This method is carried out on a particular steady-state determined by dc bias, in specified illumination conditions, and allows us to probe different positions in the J - V curve by changing dc bias. The technique shows well-resolved arcs in the complex impedance plot for electronic and ionic processes taking place at different characteristic times.^{13,14} Unfortunately, the use of impedance spectroscopy on perovskite solar cells has been challenging because of the richness of simultaneously occurring physical processes, such as transport of electron and hole charge carriers and ionic movement. For a technique such as impedance spectroscopy to be a useful tool, the data needs to be rationalized in a systematic way. The perovskite solar cell field is still in a phase of collecting more data so that a clear picture can emerge.^{15–20} For example, in data reported to date, it is generally assumed that the external contacts are highly efficient and selective to the carriers and thereby provide essentially ohmic contacts. Importantly, for the purpose of this work, the signature of the contacts has not been unambiguously identified by impedance spectroscopy.

The focus of this work is to understand and distinguish the impedance response related to the bulk of the perovskite from that from the external contacts in perovskite solar cells. We aim to find the general structure of the equivalent circuit representing the charge accumulation and transfer processes in a variety of cells with different characteristics. To this end, photovoltaic devices are analyzed by impedance spectroscopy containing electron transport layers (ETL) prepared by atomic layer deposition (ALD): SnO_2 , TiO_2 , and Nb_2O_5 . Overall, the present report provides insights into the impedance response of perovskite solar cells, which enable unambiguous understanding on the characteristic signals of the perovskite layer with those arising from the contacts.

EXPERIMENTAL SECTION

Device Preparation. F: SnO_2 substrates were first wiped with acetone and then cleaned for 10 min in piranha solution ($\text{H}_2\text{SO}_4/\text{H}_2\text{O}_2 = 3:1$) followed by 10 min in a plasma cleaner prior to ALD deposition. ALD of TiO_2 ²¹ was carried out in a Savannah ALD 100 instrument (Cambridge Nanotech Inc.) at 120 °C using tetrakis(dimethylamino)titanium(IV) (TDMAT,

99.999% pure, Sigma-Aldrich) and H_2O_2 . TDMAT was held at 75 °C and H_2O_2 at room temperature. The growth rate was 0.07 nm/cycle at a N_2 flow rate of 5 sccm as measured by ellipsometry. SnO_2 was deposited at 118 °C using tetrakis(dimethylamino)tin(IV) (TDMASn, 99.99%-Sn, Strem Chemicals INC) and ozone at a constant growth rate of 0.065 nm/cycle measured by ellipsometry. TDMASn was held at 65 °C. Ozone was produced by an ozone generator (AC-2025, IN USA, Inc.) fed with oxygen gas (99.9995% pure, Carbagas), producing a concentration of 13% ozone in O_2 . Nitrogen was used as a carrier gas (99.9999% pure, Carbagas) with a flow rate of 10 sccm. Nb_2O_5 was deposited at 170 °C and a carrier gas flow rate of 20 sccm using (*tert*-butylimido)bis(diethylamino)-Niobium (TBTDEN, Digital Specialty Chemicals, Canada) and ozone with a constant growth rate of 0.06 nm/cycle. TBTDEN was held at 130 °C.

Before perovskite deposition, the ALD layers were treated with UV ozone for 10 min to remove byproducts from the deposition process. The perovskite films were deposited from a precursor solution containing FAI (1 M), PbI_2 (1.1 M, TCI Chemicals), MABr (0.2 M), and PbBr_2 (0.22 M, AlfaAesar) in anhydrous DMF:DMSO 4:1 (v:v, Acros) (MA, methylammonium; FA, formamidinium). The perovskite solution was spin-coated in a two-step program; first at 1000 rpm for 10 s and then at 4000 rpm for 30 s. During the second step, 100 μL of chlorobenzene was poured on the spinning substrate 15 s prior to the end of the program. The substrates were then annealed at 100 °C for 1 h in a nitrogen-filled glovebox.

The spiro-OMeTAD (Merck) solution (70 mM in chlorobenzene) was spun at 4000 rpm for 20 s. The spiro-OMeTAD was doped at a molar ratio of 0.5, 0.03, and 3.3 with bis(trifluoromethylsulfonyl)imide lithium salt (Li-TFSI, Sigma-Aldrich), tris(2-(1H-pyrazol-1-yl)-4-*tert*-butylpyridine)-cobalt(III) tris(bis(trifluoromethylsulfonyl)imide) (FK209, Dyenamo), and 4-*tert*-butylpyridine (TBP, Sigma-Aldrich), respectively.^{22–24} As a last step, 70–80 nm of gold top electrode were thermally evaporated under high vacuum.

Synthesis of Pure MAPbI_3 . MAPbI_3 was synthesized according to a previously reported process by evaporation of anhydrous DMF (Sigma) in a solution containing stoichiometric amounts of lead iodide (98%) and methylammonium

iodide (TCI). The mixture was placed in an open crystallization dish at 130 °C for 3 h on a hot plate placed in fumehood; the mixture was stirred every 30 min. The black powder was characterized by X-ray diffraction (XRD) and scanning electron microscopy (SEM) to show an amorphous powder as previously reported.¹⁰ Films were prepared by pressing MAPbI₃ powders at 6 ton into a 13 mm pellet die. Amounts of the materials were varied to provide the desired thickness as evidenced by SEM images: 212 mg (350 μm), 412 mg (750 μm), and 1 g (1300 μm).

Assembly of Devices in the Configuration Pb/MAPbI₃/Pb. Symmetric devices were prepared by sandwiching a perovskite pellet between two circular Pb sheets (Alfa Aesar, 0.1 mm tick, 99.9%) with a diameter of 0.6 cm to define an active area of ~0.28 cm². The metal foil was previously treated with sand paper to remove the PbO overlayer. The materials were loaded into a HS-Flat Test Cell (Hohsen Corp.) equipped with a spring to provide adequate contacts for characterization.

Film and Device Characterization. Current density–voltage characteristics were carried out under illumination with an AM1.5G spectra (1000 W m⁻²) using an Abet Sun 2000 Solar Simulator. The light intensity was adjusted with a calibrated Si solar cell. Impedance spectroscopy measurements were performed using an Autolab PGSTAT-30 equipped with a frequency analyzer module. Measurements were carried out either in the dark or under illumination at several bias voltages.

RESULTS AND DISCUSSION

General Characterization and Photovoltaic Response.

The aim of this work is to investigate the general impedance response of perovskite (FA_{0.85}MA_{0.15}Pb(I_{0.85}Br_{0.15})₃) photovoltaic devices containing ETLs of different properties grown by ALD: SnO₂, TiO₂, and Nb₂O₅. To evaluate that the deposition procedure provides the intended perovskite structure, X-ray diffraction was measured, and a representative sample is shown in Figure 1a. The data verify the formation of a cubic perovskite with peak positions in close agreement with previously observed results.²⁵ A signal from unreacted PbI₂ is also present, as expected given the stoichiometry of the precursor solutions used in the deposition. In addition, absorption data and photoluminescence also confirm that the optical properties of the films are similar to previous results (Figure 1b). Figure 1c shows device efficiency of a fresh device with a power conversion efficiency (PCE) ≈ 17%. Note that the current world record (PCE = 21%) is based on an architecture where a thin layer of mesoporous TiO₂ is deposited on top of the electron-selective layer. The cells without mesoporous TiO₂ here investigated do not reach the same efficiency, but they are not far behind and the planar geometry greatly simplifies the interpretation of the impedance data. A top view SEM image of a representative film is given in Figure 1d where it can be observed that the film is rather uniform and that the number of microscopic pin-holes is low. Figure 1e shows a cross-sectional image of a typical device, and Figure 1f shows a photo of a complete device. Therefore, the deposition of the ETL by ALD is compatible with the achievement of high-quality perovskite films with few pin-holes and good control of the layer thickness.

Photovoltaic devices are further characterized by their stabilized *J–V* curves (Figure 2a) measured 1–2 months after device fabrication and just before impedance spectroscopy analysis; a summary of the data is collected in Table 1. All devices present some hysteresis, and for simplicity, reported

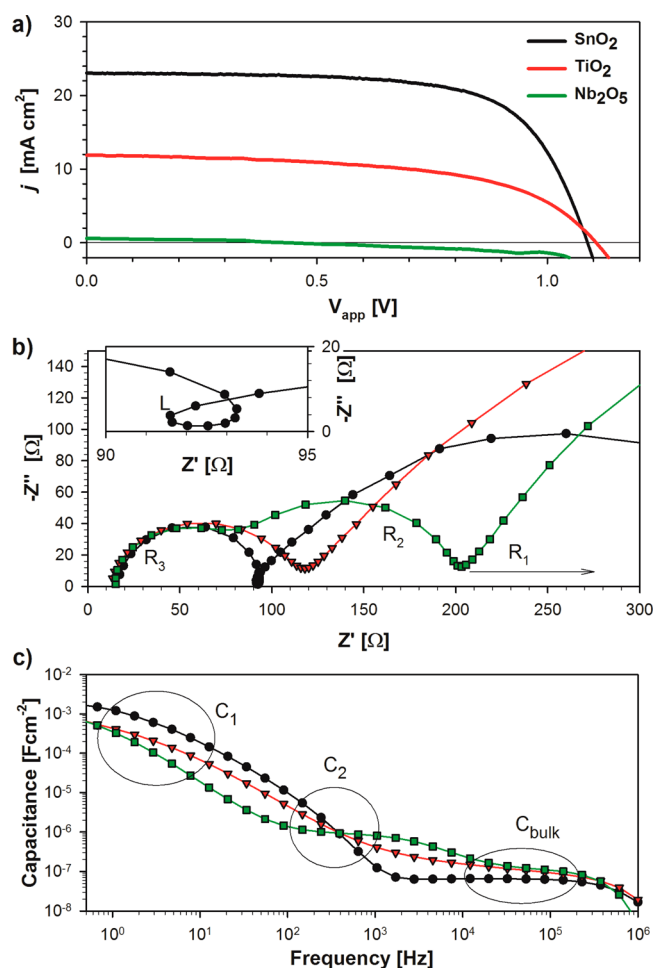


Figure 2. (a) *J–V* curves of devices 1 (SnO₂), 2 (TiO₂), and 3 (Nb₂O₅), see Table 1, measured at 1 sun light intensity prepared with different electron transport layers. (b) Complex impedance plot and (c) capacitance–frequency plot for devices measured at 1 sun light intensity at short-circuit conditions. The high-frequency region clearly depends on the oxide properties. The inset in Figure 1b shows the inductive effect observed for the high-performance devices based on a SnO₂ ETL.

Table 1. Summary of Efficiency of Devices Discussed in This Work^a

device	ETL	ETL thickness [nm]	<i>J</i> _{sc} [mA/cm ²]	<i>V</i> _{oc} [V]	FF	PCE [%]
1	SnO ₂	15	23.06	1.09	0.68	16.92
2	TiO ₂	5	11.60	1.08	0.78	9.83
3	Nb ₂ O ₅	15	0.60	0.41	0.42	0.11
4	SnO ₂	5	20.01	1.08	0.61	13.30
5	SnO ₂	100	21.62	1.05	0.45	10.23
6	TiO ₂	100	5.69	1.00	0.51	4.20

^aOnly measurements carried out at reverse bias direction are quoted for simplicity.

values correspond to measurements carried out from positive to negative bias (reverse). Optimized SnO₂ thickness of 15 nm enables efficiencies as high as ~17% (device 1, Table 1). Cells with TiO₂ (device 2) showed reduced efficiencies mainly due to low photocurrents. An ETL of Nb₂O₅ (device 3) results in very low device efficiencies due to both low photocurrents and fill factors (FF). Therefore, TiO₂ and Nb₂O₅ contacts produce progressively lower device efficiencies. Alternatively, if the SnO₂

layer thickness is reduced to 5 nm (device 4), lower photocurrent and FF than device 1 is observed. This reduced performance can partly be ascribed to the presence of pinholes. As a general guideline, increasing the thickness of the ETL reduces the FF because of increase of the contact resistance (devices 5 and 6).

Impedance Response of Optimized Devices Using Different ETLs. Characteristic impedance response measured at 1 sun light intensity of perovskite solar cells containing different types of electron transport layer is shown in Figure 2. We will use two main types of representation to analyze the data. One is the complex impedance plot, Figure 2b, which reveals different arcs when the processes are well-separated with respect to frequency. This is an important method to identify the dynamic features of the system. The complex impedance plot (Z' , $-Z''$) directly shows resistance values by measuring the width of arc in the real axis. Alternatively, another important representation is the capacitance–frequency (C – f) plot that shows the general evolution of capacitive processes, see Figure 2c. Note that the capacitance representation is just a rephrasing of the impedance data. Complex capacitance is defined as

$$C(\omega) = \frac{1}{i\omega Z(\omega)} \quad (1)$$

Here, ω is the angular frequency related to the frequency as $f = \omega/2\pi$. Represented in Figure 2c is the real part of the complex capacitance. This is a general view of the capacitive response, but specific capacitive processes, and the quantitative capacitance value, need to be obtained by fitting to an equivalent circuit model. On the other hand, if capacitance traces different plateaus, each corresponding to separate polarization processes, one can directly identify specific capacitive processes in the C – f plot.²⁶

In the case of the best performing sample, with SnO₂ contact, two arcs can be observed in the complex impedance plots of Figure 2b, with different characteristic frequencies. For clarity in Figure 2b, the low-frequency arc resistance is denoted as R_1 and the high-frequency arc as R_3 . The capacitance shows two main features. At high frequency we observe a capacitive plateau in the range of $0.1 \mu\text{F cm}^{-2}$ that is rather insensitive to the light intensity, and it will be associated below to the intrinsic dielectric polarization of the perovskite layer. This capacitance that we term C_{bulk} is due to diverse dipolar mechanisms as previously reported:²⁶ CH₃NH₃⁺ or PbI₆ octahedra reorientation, and cooperative ionic off-centering. On the other hand, in the low-frequency range of Figure 2c, we obtain the giant capacitance that has been observed in several previous reports,^{27–30} and it will be termed here C_1 . Note that this capacitance corresponds to the low-frequency arc in complex impedance plot R_1 . In the dark conditions, this feature is related to the electrode polarization taking place as a consequence of ion migration to the electrodes and charge compensation by the external electrodes.²⁶ The low-frequency capacitance grows to high values under illumination and markedly depends on type of contact; therefore, it is believed that this feature is associated with electronic and ionic accumulation at the electrode interfaces.²⁸ Recently, a detailed analysis of thickness, illumination, and bias voltage dependence indicated that the large capacitance C_1 under illumination is caused by an electron accumulation layer at the interface.³¹ Finally, in the transition region between the two arcs, an inductive effect appears for

high-performance devices (SnO₂), which manifests as a loop (inset in Figure 2b) in the complex plane plot.

An additional arc develops when the lower performing oxides are compared to a good extraction layer in the high-frequency region. For TiO₂ (device 2), a distorted arc is observed in the high-frequency region, which appears to be the coupling of two processes. Alternatively, for Nb₂O₅ (device 3), a new arc (R_2) is very well resolved so that three separate arcs can be observed. Similarly, a new capacitive process indicated by intermediate-frequency (1–10 kHz) plateau appears in the capacitance–frequency plot (Figure 2c). Note that this capacitance cannot be ascribed to a geometrical capacitance of the contact. A 5 nm layer of TiO₂ with $\epsilon \sim 20$ would provide a dielectric capacitance of about 10 mF/cm^2 , which is far higher than the observed value of $\sim 1\text{--}5 \mu\text{F/cm}^2$. Instead, the capacitance appears to be related to the interfacial accumulation of carriers at one interface, as will be discussed below.

In Figure 3, impedance data measured under 1 sun illumination and short circuit conditions is given for devices

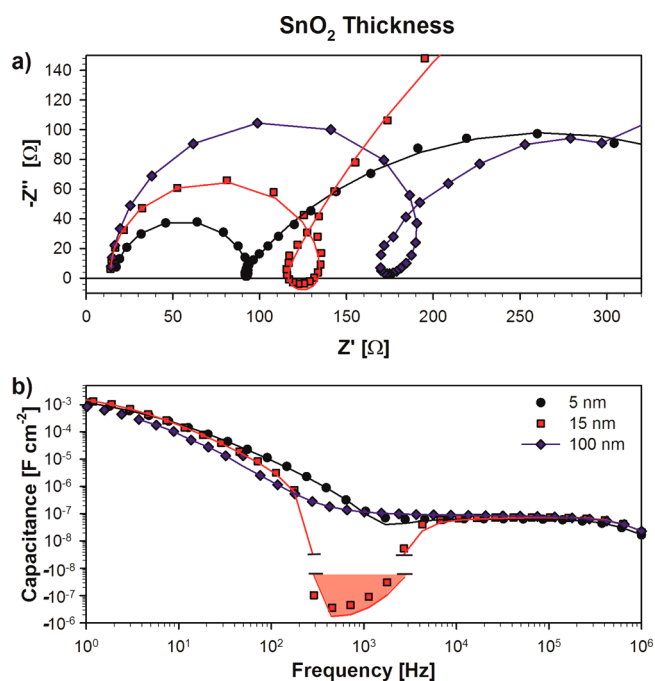


Figure 3. Complex impedance plane (a) and capacitance–frequency plots (b) of devices containing SnO₂ as ETL with different thicknesses measured at 1 sun light intensity. Solid lines correspond to fitting values using the complete equivalent circuit in Scheme 1C. The negative capacitance region is shown in red.

with three different thicknesses of SnO₂. As can be observed, the size of the arc, here termed R_3 , scales with the thickness of the ETL layer and gets smaller for thinner layers. Therefore, it can be concluded that the high-frequency arc depends heavily on the transport resistance of the ETL layer but the associated capacitance in Figure 3b corresponds to the bulk properties of the perovskite layer, as shown below. This signal can, however, be obscured by C_2 in less efficient contacts, such as TiO₂ or Nb₂O₅ deposited by ALD, see Figure 2c.

Figure 3 also shows the inductive loop at intermediate frequencies to be highly thickness-dependent. Importantly, the inductive effect has been observed in all high-performing solar cells analyzed so far. Poorly performing solar cells fabricated without selective contacts, such as those with the configuration

FTO/perovskite/Au, also show the inductive effect as illustrated in the [Supporting Information](#).³² Hence, the inductive loop is a broadly observed feature, and we believe that the absence of observation of the inductive feature is a clear sign for charge accumulation at the perovskite/contact interface.

Response of Bulk Properties of the Perovskite Layer.

Insight to the physical interpretation of capacitances is a major step in the application of impedance spectroscopy to understand the physical characteristics of solar cells. We now focus our attention on the high-frequency plateau of [Figures 2c](#) and [3c](#). For a suitable interpretation, we measure the impedance of devices of different thicknesses of the perovskite absorber (d), which is very useful to reveal the nature of capacitance. A series of complete devices (diode structure with asymmetric selective contacts) with a perovskite layer of 350 nm are compared with symmetric devices (Pb/MAPbI₃/Pb) of much larger thicknesses (between 350 μm and 1.3 mm). In [Figure 4](#), complex impedance plane and C - f plots are shown of devices fabricated spanning perovskite thicknesses of several orders of magnitude measured under dark conditions and applied bias of 0 V. We obtain that the plateau at high frequency clearly scales with the thickness of the perovskite layer as a typical parallel

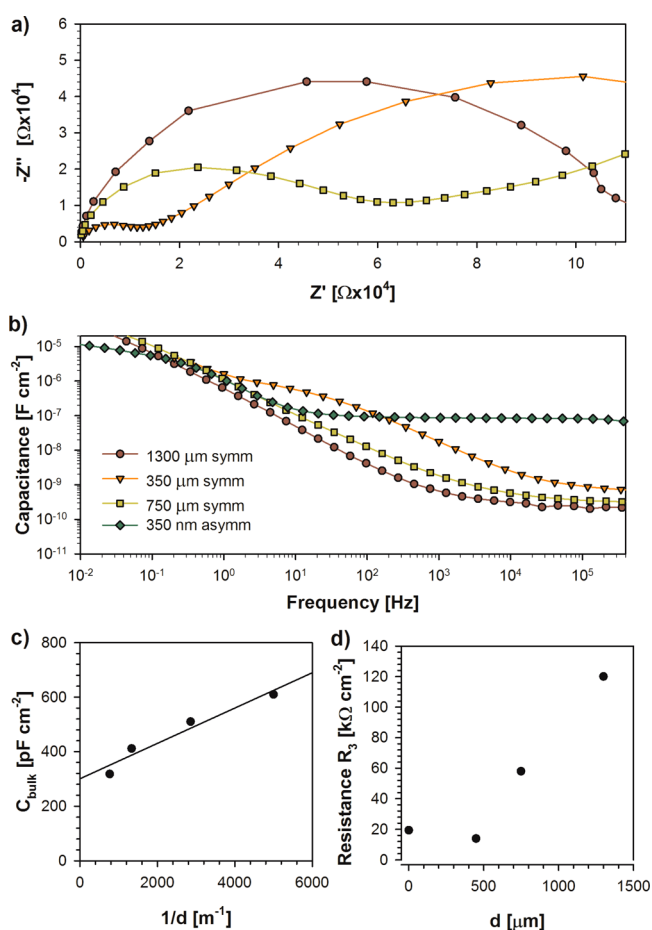


Figure 4. Complex impedance plot (a) and C - f (b) including symmetric devices fabricated with pellets using perovskite materials with different thickness and measured under dark conditions and at $V_{\text{dc}} = 0$ V. A working photovoltaic device with asymmetric contacts and an active layer thickness of 350 nm is included for comparison. (c) Capacitance and (d) resistance dependence on perovskite layer thickness.

plate capacitor in which the capacitance per unit area is inversely proportional to the thickness ($C = \epsilon\epsilon_0/d$), where ϵ_0 is the permittivity of vacuum. [Figure 4c](#) shows the linear dependence of capacitance with respect to d^{-1} . The capacitance of the device at this high frequency (83 nF/cm^{-2}) can be used to calculate the dielectric constant, ϵ , of the perovskite thin film in devices to provide a value of 23.³³ Alternatively, a relative dielectric constant of the perovskite layer of 37 can be calculated from the slope of the straight line using the data points corresponding to the pellets. This high value is not really surprising because the pellets are prepared from compacting crystalline bulk perovskite to provide a very different morphology. In addition, we note that some remaining capacitance from the intermediate-frequency response is still present as the intercept with the y -axis is not zero as would be expected from a pure geometric capacitance. Previous results using Au contacts with pellets have provided values of the dielectric constant of 22.³⁴

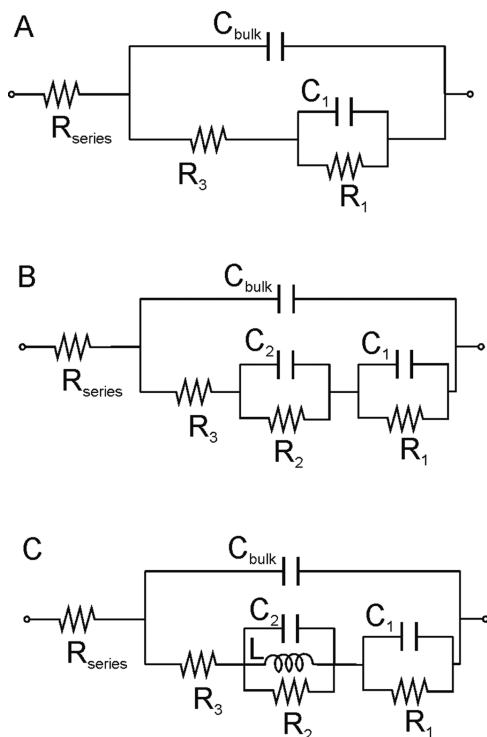
With respect to high-frequency resistance (R_3) of the samples, a qualitative trend for the symmetric samples can be observed in which the size of the high-frequency arc decreases by decreasing the thickness of the perovskite layer, which indicates a relationship of R_3 with the transport resistance of the perovskite layer for symmetric samples. However, in asymmetric contact devices with a perovskite thickness of 350 nm, the resistance measured under dark conditions is very similar to that of a pellet with 350 μm . Therefore, the linearity is maintained only to a certain degree because R_3 also depends on the resistivity of the contacts, as shown in [Figure 3a](#), and the effect of the contact will be more remarkable as we reduce the perovskite layer thickness.

Equivalent Circuit Models. A very simple equivalent circuit that accounts for the physical processes taking place in a high-performance solar cell is represented in [Scheme 1A](#). In this model, the resistance R_3 is coupled to C_{bulk} , which corresponds to the high-frequency arc. R_1 and C_1 represent the parameters associated with the contacts to the perovskite.¹⁷ This second arc contribution gives the large capacitance, C_1 , at the low frequency observed in [Figure 2c](#). The simple circuit A has been a common assumption in previous work with contacts showing good properties and high efficiency.^{30,35–37}

According to the previous analysis, the capacitance C_{bulk} is mainly associated with the intrinsic dielectric relaxation of the bulk perovskite layer. More generally, depending on temperature and other external variables, this capacitance is dominated by the geometric capacitance and may contain components of contact layers responding in a very high-frequency domain.²⁶ The element R_3 may in the standard picture correspond to the conductivity of the bulk perovskite, but we have noted in [Figure 3](#) that the high-frequency arc resistance, R_3 , is heavily influenced by the contact transport resistance. In summary, under the conditions of measurement adopted in this paper, we identify the element C_{bulk} with the bulk capacitance of the perovskite layer, as was shown in [Figure 2](#).

Although circuit A in many cases is sufficient to describe the experimental data, we could here, by using a variety of contacts as well as modifying their thickness, reveal new features that indicate the origin of the impedance features in more detail. We have already noted an evolution of the impedance spectra, from two arcs with the best performing contacts toward three arcs for less efficient devices, which has also been previously observed.³⁸ In [Scheme 1B](#), we propose a new equivalent circuit to account for this general observation. In this more general

Scheme 1. (A) Equivalent Circuit for the Analysis of Perovskite Solar Cells Consisting of Bulk and Interface Components, (B) Advanced Circuit with Extended Interfacial Structure, and (C) Advanced Circuit to Account for Inductive Effect



circuit, the previous structure associated with the interface, R_1C_1 , is replaced by a more elaborate structure allowing for additional kinetic and charge storage processes occurring at the interface represented by elements R_2 and C_2 . This model can be applied to describe devices with less efficient external contacts. Obviously, the new elements introduce a third arc situated in the middle-frequency range, as shown in the simulations in Figure 5. In the C - f plot, the element C_2 introduces a new capacitance plateau in the intermediate-frequency range. Therefore, only C_{bulk} depends on the bulk capacitance of perovskite layer, and all the other elements are largely dependent on the contact properties. This is a model allowing for an extremely complex structure of charge accumulation and transfer at the external interfaces in perovskite solar cells. This model is in agreement with a recent report that suggest that long time modifications such as noncapacitive hysteresis behavior can be mainly associated with the modification of injection barriers at the external interfaces of the perovskite absorber.⁹

It has been remarked that the best performing cells using a SnO_2 contact display only two arcs in Figure 2b, which at first sight could accurately be described by model circuit A. A more detailed inspection of the data and a variation of contact thickness does, however, indicate an impedance loop at intermediate frequencies of the spectra, as seen in the inset of Figure 2b, which occurs instead of the intermediate-frequency arc (R_2C_2) that appears for worse performing contacts. This result indicates that both circuits A and B are not yet complete and that additional physical features need to be considered.

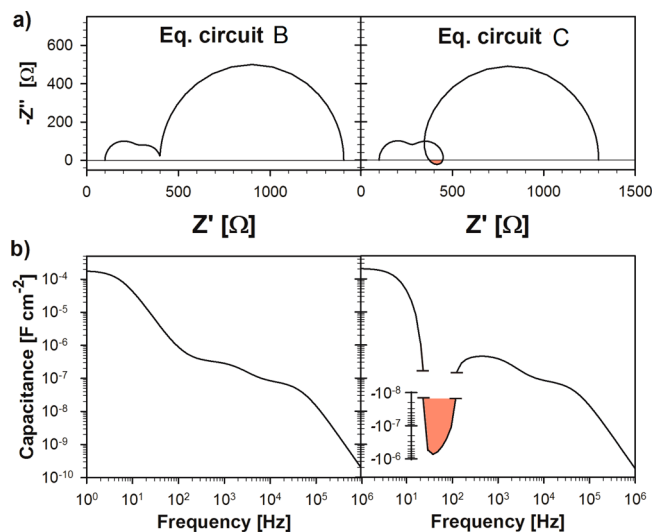


Figure 5. (a) Simulation of complex impedance plot and (b) capacitance–frequency plot for the extended circuits in Scheme 1B,C. Parameters values are given in the Supporting Information. The area marked in red corresponds to negative capacitance values.

Impedance loops are commonly associated with negative capacitance in solar cells.^{39,40} This feature is widely reported as a loop crossing to negative capacitance at extreme low frequencies, which is a rather common occurrence in electrochemistry.⁴¹ In the same way it has also been observed in hybrid perovskite solar cells.^{15,19} However, the loop observed in Figure 3a is a different type of phenomenon, as it occurs at intermediate frequencies. We are not aware of precedents of a similar signature in any type of solar cells. However, it is often found in battery materials,^{42,43} which are ionic conductors, similar to hybrid perovskite. In Scheme 1C, we show an advanced equivalent circuit able to describe this loop. In this circuit, the parallel R_2C_2 -element in Scheme 1b has been expanded to a more complex subcircuit that includes an inductor, L . As the impedance of the inductor is $Z = i\omega L$, the inductor acts as a short at low frequency, which reduces the impedance for charge transfer. Consider a parallel connection of capacitor and inductor, with impedance

$$Z = \left(i\omega C_2 + \frac{1}{i\omega L} \right)^{-1} = \frac{1}{i\omega} \frac{1}{\left(C_2 - \frac{1}{\omega^2 L} \right)} \quad (2)$$

In the intermediate-frequency range, the loop is produced by the new subcircuit (R_2C_2L) as shown in the simulations in Figure 5. The inductor has the ability to decrease the effect of the upper branch C_2 of the interfacial impedance and can provide a negative capacitance, indicated as the red region in Figure 5. Indeed, the middle arc may be completely removed by effect of this inductor, as observed in the experimental data (Figure 2). Devices showing all the features are rarely observed because R_2 and C_2 usually mask the inductive effect. In the Supporting Information, an example of a cell with all the features of the equivalent circuit C is shown corresponding to device 6 (TiO_2 , 100 nm) measured under light and a bias close to V_{oc} .

Inductive loops in impedance spectroscopy are associated with complex multistep dynamics. In the analysis of electronic devices, such as solar cells and LEDs, it is often associated with surface states.⁴⁰ This negative capacitance indicates a strong

interaction between thermodynamic and kinetic features of an intermediate electronic state, whereby an increase of the Fermi level modifies the rates of charge transfer and enables emptying of the electronic state.⁴⁰ Therefore, the inductive feature provides a nonlinear accelerated kinetics of an intermediate state. Another related approach has been developed in ref 35, in which the low-frequency capacitance is carrier density-dependent.

It is beyond the scope of the current paper to identify the precise physical meaning of all the equivalent circuit model elements that have been found necessary to describe the impedance spectra, especially those in the intermediate-frequency range. This task will require further studies combining different techniques. To summarize the results obtained so far we should, however, remark that the complexity of the interfacial charge-transfer process quantitatively is represented by the lower branch of the equivalent circuit in Scheme 1C. When the solar cell is optimized to provide large power conversion efficiency, the charge-transfer process still consists of a serial combination of several processes, including an inductive element. The fact that most of the resistance is associated with contact effects indicates that the recombination resistance associated with the dominant recombination process in the solar cell must occur predominantly at the contacts, and very probably via intraband localized states. Note that all the impedance data shown in this paper has been successfully fitted using the equivalent circuits B or C depending on whether the loop is visible or not, see Figures 2 and 3. Therefore, a quantitative analysis can be carried out to gain more understanding on device operation as will be shown in the last section.

Effect of Light in the Capacitance Response: Masking of Bulk Capacitance. In the following set of experiments we analyze the dependence of capacitance with the illumination intensity. In Figure 6, the champion device (device 1, PCE = 17%) is compared with a device containing a thick layer of TiO₂ (device 6, PCE = 4.2%), which we recall from the preceding analysis showed issues with charge transfer at the

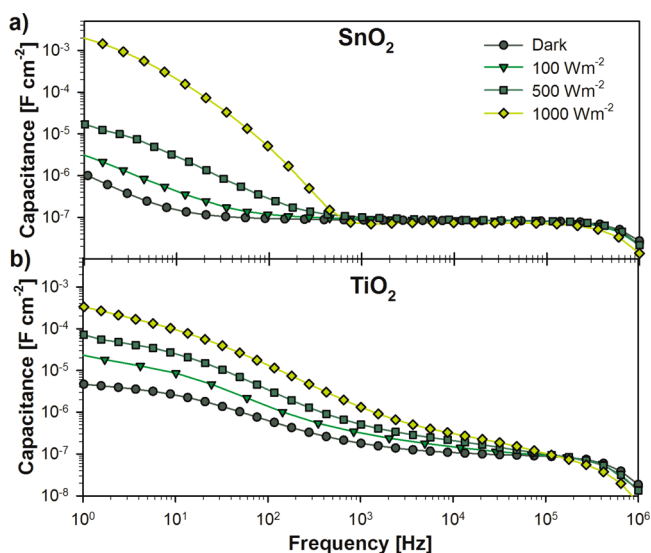


Figure 6. Capacitance–frequency plots of devices containing two different ETL oxide layers measured at different light intensities: (a) a good extraction layer of SnO₂ (15 nm) and (b) device containing a thick layer of TiO₂ (100 nm).

perovskite/ETL interface. Some important new features emerge in this comparison. The additional capacitance (C_2) observed for a device containing a thick layer of TiO₂ overlaps at high frequency the bulk capacitance of the perovskite layer, Figure 6b. Under illumination, the increase of capacitance extends into very high frequency and the whole spectrum is modified by the effect of photogenerated carriers. This is the typical behavior that has been repeatedly observed with nanostructured or rough contacts.^{27,29} In contrast to this, for the SnO₂ sample in Figure 6a, the high-frequency plateau is remarkably stable and independent of illumination over a broad range of frequencies starting at 10³ Hz. Thus, one is able to unambiguously separate capacitive bulk and contact effects in the perovskite solar cell in this case.

Connection between Charge Accumulation at the ETL/Perovskite Interface and Photocurrent Reduction.

Once the general features of the impedance response have been assigned and justified, we can further analyze the solar cells containing different oxides as ETLs using the fitting results from the advanced equivalent circuit shown in Scheme 1C. In Figure 7 we pay attention to the high-frequency region by

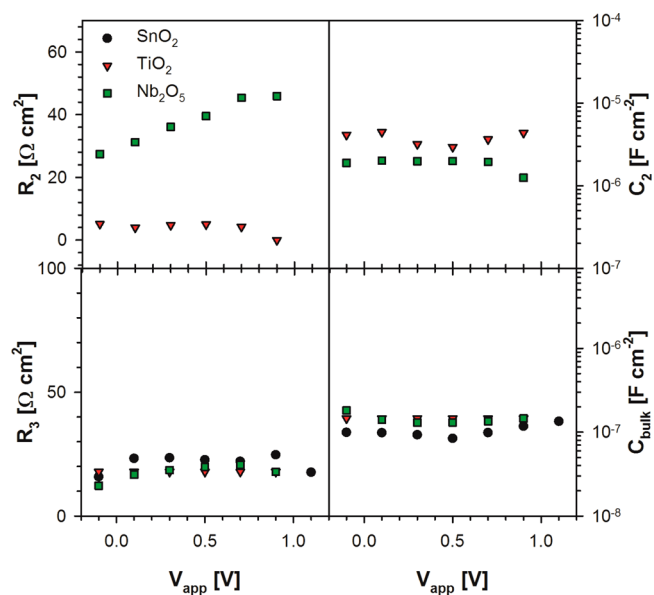


Figure 7. Fitting results for the bulk and interfacial features present in devices shown in Figure 1.

analyzing the fitting values for R_3 and C_{bulk} , and we observe that these values are almost the same for the three samples containing the different oxides. These results confirm that the perovskite layer prepared in the series of samples is very similar for the different devices. On the other hand, the new feature appearing at intermediate frequencies is the most different attribute for the three samples. This accumulation of photogenerated carriers has been ascribed to the interfacial capacitance and resistance associated with the perovskite/ETL interface. In terms of the J – V response, the main difference between the three samples is the difference in photocurrent which decays from 23 to 0.6 mA/cm² when SnO₂ (device 1) is compared to Nb₂O₅ (device 3). Such a decrease of current cannot be explained by any type of series resistance internal to the ETL because of poor conductivity, which would change the fill factor but not photocurrent. The impedance associated with the transfer of carriers promotes the charge

accumulation at the interface and ultimately enhances interfacial recombination, which dramatically reduces the extracted photocurrent. A recent work has shown by detailed modeling and experiment that surface recombination is a central effect causing reduction of photocurrent.⁴⁴

At present an interpretation of the two separate capacitive elements C_1 and C_2 attributed to interfacial response cannot be safely established. However, according to the previous knowledge, the low-frequency large capacitance C_1 contains mainly ionic double-layer components in the dark, and increases under light by an electronic contribution of photogenerated carrier accumulation at the interface perovskite/ETL.^{26,31} Therefore, we may tentatively associate the intermediate capacitive process C_2 (visible as a plateau in Figure 1c for Nb₂O₅ contact) to an additional electronic surface state that has a large impact on recombination. Low-frequency capacitances have rather disparate values according to the type of contact. Beyond ionic double-layer and electronic accumulation effects, other phenomena related to the specific surface of the perovskite, such as the surface reconstruction and enhanced polarity,⁴⁵ may play an important role in the operation of the interface.

In summary the extraction of carriers at the contacts seems to provide the dominant impedance response of the solar cells investigated here. Elements C_{bulk} and R_3 contain predominantly the contribution of the bulk perovskite layer to the cell impedance, even though series resistance of contact may contribute as well to R_3 , as evidenced in Figure 3a. Then, there appears a very complex structure of impedance elements associated with the interfacial impedance at the contact between perovskite and electron or hole extraction layer material. This contribution is represented by elements 1 and 2 in the equivalent circuit of Scheme 1C. Such structure indicates a serial process of electron transfer steps while the interface is also influenced by ionic double-layer capacitance and additional electronic capacitance representing surface states and the accumulation of carriers at the contact. The recombination resistance appears to be contained in these interfacial elements, but a clear separation of R_{rec} is not possible at this stage. We do not claim that this equivalent circuit is complete or represents all possible processes in a perovskite solar cell. For example, there is evidence for transport elements in some cases that will introduce Warburg diffusion or additional transport resistances.^{16,18,20} The terminal low-frequency negative capacitance has been also broadly observed.^{15,19} However, the present contribution is a robust framework for the interpretation of the central elements that compose the rather intricate impedance response of perovskite solar cells, including high performance cells, as well as for the determination of degradation of the contacts by prolonged operation.¹¹

CONCLUSIONS

The present report provides insights into the impedance response of perovskite solar cells, which enable unambiguous understanding of the operational principles. The geometrical capacitance of the perovskite layer is observed in the high-frequency region. However, this can be masked under illumination if an inefficient ETL is used. On the other hand, the resistance of the high-frequency response depends on both conductivity of perovskite layer and contacts. Alternatively, if an inefficient extraction layer is used, such as ALD deposited TiO₂ or Nb₂O₅, a new arc appears in the intermediate-frequency region. This arc is highly coupled with the properties of the perovskite layer, and it is related with increased recombination

processes. It is generally observed that interfacial recombination dominates the impedance response. In the low-frequency region we find the signature of electronic and ionic accumulation at the contact interface. Finally, we revealed an inductive element at intermediate frequencies. This feature is characteristic but not exclusive to high-performance devices. Failure of observation of the inductive feature is a sign for charge accumulation at the perovskite/contact interface. Thus, one is able to separate bulk and contact effects in the perovskite solar cell in this case.

ASSOCIATED CONTENT

Supporting Information

The Supporting Information is available free of charge on the ACS Publications website at DOI: 10.1021/acs.jpcc.6b01728.

SEM images, J - V curves, and impedance plots of perovskite cells displaying loops (PDF)

AUTHOR INFORMATION

Corresponding Authors

*E-mail: aguerrer@uji.es. Tel.: +34 964727555.

*E-mail: bisquert@uji.es. Tel.: +34 964727541.

*E-mail: anders.hagfeldt@epfl.ch. Tel.: +41 21 69 35308.

Notes

The authors declare no competing financial interest.

ACKNOWLEDGMENTS

The work at INAM-UJI was supported by Generalitat Valenciana project PROMETEO/2014/020 and MINECO of Spain under Project MAT2013-47192-C3-1-R. A.G. thanks the Spanish Ministerio de Economía y Competitividad for a Ramón y Cajal Fellowship (RYC-2014-16809). T.J.J. gratefully acknowledges the GRAPHENE project supported by the European Commission Seventh Framework Program under Contract 604391.

REFERENCES

- (1) Burschka, J.; Pellet, N.; Moon, S.-J.; Humphry-Baker, R.; Gao, P.; Nazeeruddin, M. K.; Grätzel, M. Sequential deposition as a route to high-performance perovskite-sensitized solar cells. *Nature* **2013**, *499*, 316–319.
- (2) Lee, M. M.; Teuscher, J.; Miyasaka, T.; Murakami, T. N.; Snaith, H. J. Efficient hybrid solar cells based on meso-superstructured organometal halide perovskites. *Science* **2012**, *338*, 643–647.
- (3) Zhou, H.; Chen, Q.; Li, G.; Luo, S.; Song, T.-b.; Duan, H.-S.; Hong, Z.; You, J.; Liu, Y.; Yang, Y. Interface engineering of highly efficient perovskite solar cells. *Science* **2014**, *345*, 542–546.
- (4) Green, M. A.; Emery, K.; Hishikawa, Y.; Warta, W.; Dunlop, E. D. Solar cell efficiency tables (Version 45). *Prog. Photovoltaics* **2015**, *23*, 1–9.
- (5) Yang, W. S.; Noh, J. H.; Jeon, N. J.; Kim, Y. C.; Ryu, S.; Seo, J.; Seok, S. I. High-performance photovoltaic perovskite layers fabricated through intramolecular exchange. *Science* **2015**, *348*, 1234–1237.
- (6) Jeon, N. J.; Noh, J. H.; Yang, W. S.; Kim, Y. C.; Ryu, S.; Seo, J.; Seok, S. I. Compositional engineering of perovskite materials for high-performance solar cells. *Nature* **2015**, *517*, 476–480.
- (7) Bi, D.; Tress, W.; Dar, M. I.; Gao, P.; Luo, J.; Renevier, C. m.; Schenk, K.; Abate, A.; Giordano, F.; Correa Baena, J. P.; Decoppet, J.-D.; Zakeeruddin, S. M.; Nazeeruddin, M. K.; Grätzel, M.; Hagfeldt, A. Efficient luminescent solar cells based on tailored mixed-cation perovskites. *Science Advances* **2016**, *2*, e1501170.
- (8) Xiao, Z.; Yuan, Y.; Shao, Y.; Wang, Q.; Dong, Q.; Bi, C.; Sharma, P.; Gruverman, A.; Huang, J. Giant switchable photovoltaic effect in

organometal trihalide perovskite devices. *Nat. Mater.* **2014**, *14*, 193–198.

(9) Chen, B.; Yang, M.; Zheng, X.; Wu, C.; Li, W.; Yan, Y.; Bisquert, J.; Garcia-Belmonte, G.; Zhu, K.; Priya, S. Impact of capacitive effect and ion migration on the hysteretic behavior of perovskite solar cells. *J. Phys. Chem. Lett.* **2015**, *6*, 4693–4700.

(10) Carrillo, J.; Guerrero, A.; Rahimnejad, S.; Mas-Marza, E.; Bisquert, J.; Garcia-Belmonte, G. Ionic reactivity at contacts and aging of methylammonium lead triiodide perovskite solar cell. *Adv. Energy Mater.* **2016**, DOI: 10.1002/aenm.201502246.

(11) Guerrero, A.; You, J.; Aranda, C.; Kang, Y. S.; Garcia-Belmonte, G.; Zhou, H.; Bisquert, J.; Yang, Y. Interfacial degradation of planar lead halide perovskite solar cells. *ACS Nano* **2016**, *10*, 218–224.

(12) Bisquert, J.; Fabregat-Santiago, F. Dye-Sensitized Solar Cells. In *Impedance Spectroscopy: A General Introduction and Application to Dye-Sensitized Solar Cells*; Kalyanasundaram, K., Ed.; CRC Press: Boca Raton, FL, 2010.

(13) Fabregat-Santiago, F.; Garcia-Belmonte, G.; Mora-Seró, I.; Bisquert, J. Characterization of nanostructured hybrid and organic solar cells by impedance spectroscopy. *Phys. Chem. Chem. Phys.* **2011**, *13*, 9083–9118.

(14) Bisquert, J.; Fabregat-Santiago, F. Impedance Spectroscopy: A general Introduction and Application to Dye-Sensitized Solar Cells. In *Dye-sensitized solar cells*; Kalyanasundaram, K., Ed.; CRC Press: Boca Raton, FL, 2010.

(15) Sanchez, R. S.; Gonzalez-Pedro, V.; Lee, J.-W.; Park, N.-G.; Kang, Y. S.; Mora-Sero, I.; Bisquert, J. Slow dynamic processes in lead halide perovskite solar cells. Characteristic times and hysteresis. *J. Phys. Chem. Lett.* **2014**, *5*, 2357–2363.

(16) Gonzalez-Pedro, V.; Juarez-Perez, E. J.; Arsyad, W.-S.; Barea, E. M.; Fabregat-Santiago, F.; Mora-Sero, I.; Bisquert, J. General working principles of $\text{CH}_3\text{NH}_3\text{PbX}_3$ perovskite solar cells. *Nano Lett.* **2014**, *14*, 888–893.

(17) Pascoe, A. R.; Duffy, N. W.; Scully, A. D.; Huang, F.; Cheng, Y.-B. Insights into Planar $\text{CH}_3\text{NH}_3\text{PbI}_3$ Perovskite Solar Cells Using Impedance Spectroscopy. *J. Phys. Chem. C* **2015**, *119*, 4444–4453.

(18) Bag, M.; Renna, L. A.; Adhikari, R. Y.; Karak, S.; Liu, F.; Lahti, P. M.; Russell, T. P.; Tuominen, M. T.; Venkataraman, D. Kinetics of ion transport in perovskite active layers and its implications for active layer stability. *J. Am. Chem. Soc.* **2015**, *137*, 13130–13137.

(19) Zohar, A.; Kedem, N.; Levine, I.; Zohar, D.; Vilan, A.; Ehre, D.; Hodes, G.; Cahen, D. Impedance spectroscopic indication for solid state electrochemical Reaction in $(\text{CH}_3\text{NH}_3)\text{PbI}_3$ films. *J. Phys. Chem. Lett.* **2016**, *7*, 191–197.

(20) Dualeh, A.; Moehl, T.; Tétreault, N.; Teuscher, J.; Gao, P.; Nazeeruddin, M. K.; Grätzel, M. Impedance spectroscopic analysis of lead iodide perovskite-sensitized solid-state solar cells. *ACS Nano* **2014**, *8*, 362–373.

(21) Azevedo, J.; Steier, L.; Dias, P.; Stefik, M.; Sousa, C. T.; Araujo, J. P.; Mendes, A.; Graetzel, M.; Tilley, S. D. On the stability enhancement of cuprous oxide water splitting photocathodes by low temperature steam annealing. *Energy Environ. Sci.* **2014**, *7*, 4044–4052.

(22) Abate, A.; Leijtens, T.; Pathak, S.; Teuscher, J.; Avolio, R.; Errico, M. E.; Kirkpatrick, J.; Ball, J. M.; Docampo, P.; McPherson, I.; Snaith, H. J. Lithium salts as “redox active” p-type dopants for organic semiconductors and their impact in solid-state dye-sensitized solar cells. *Phys. Chem. Chem. Phys.* **2013**, *15*, 2572–2579.

(23) Abate, A.; Staff, D. R.; Hollman, D. J.; Snaith, H. J.; Walker, A. B. Influence of ionizing dopants on charge transport in organic semiconductors. *Phys. Chem. Chem. Phys.* **2014**, *16*, 1132–1138.

(24) Snaith, H. J.; Abate, A.; Ball, J. M.; Eperon, G. E.; Leijtens, T.; Noel, N. K.; Stranks, S. D.; Wang, J. T.-W.; Wojciechowski, K.; Zhang, W. Anomalous Hysteresis in Perovskite Solar Cells. *J. Phys. Chem. Lett.* **2014**, *5*, 1511–1515.

(25) Correa Baena, J. P.; Steier, L.; Tress, W.; Saliba, M.; Neutzner, S.; Matsui, T.; Giordano, F.; Jacobsson, T. J.; Srimath Kandada, A. R.; Zakeeruddin, S. M.; Petrozza, A.; Abate, A.; Nazeeruddin, M. K.; Grätzel, M.; Hagfeldt, A. Highly efficient planar perovskite solar cells

through band alignment engineering. *Energy Environ. Sci.* **2015**, *8*, 2928–2934.

(26) Almora, O.; Zarazua, I.; Mas-Marza, E.; Mora-Sero, I.; Bisquert, J.; Garcia-Belmonte, G. Capacitive dark currents, hysteresis, and electrode polarization in lead halide perovskite solar cells. *J. Phys. Chem. Lett.* **2015**, *6*, 1645–1652.

(27) Juarez-Perez, E. J.; Sanchez, R. S.; Badia, L.; Garcia-Belmonte, G.; Kang, Y. S.; Mora-Sero, I.; Bisquert, J. Photoinduced giant dielectric constant in lead halide perovskite solar cells. *J. Phys. Chem. Lett.* **2014**, *5*, 2390–2394.

(28) Kim, H.-S.; Jang, I.-H.; Ahn, N.; Choi, M.; Guerrero, A.; Bisquert, J.; Park, N.-G. Control of I-V Hysteresis in $\text{CH}_3\text{NH}_3\text{PbI}_3$ Perovskite Solar Cell. *J. Phys. Chem. Lett.* **2015**, *6*, 4633–4639.

(29) Li, L.; Wang, F.; Wu, X.; Yu, H.; Zhou, S.; Zhao, N. Carrier-Activated Polarization in Organometal Halide Perovskites. *J. Phys. Chem. C* **2016**, *120*, 2536–2541.

(30) Yang, T.-Y.; Gregori, G.; Pellet, N.; Grätzel, M.; Maier, J. The significance of ion conduction in a hybrid organic–inorganic lead-iodide-based perovskite photosensitizer. *Angew. Chem., Int. Ed.* **2015**, *54*, 7905–7910.

(31) Zarazua, I.; Bisquert, J.; Garcia-Belmonte, G. Light-induced space-charge accumulation zone as photovoltaic mechanism in perovskite solar cells. *J. Phys. Chem. Lett.* **2016**, *7*, 525–528.

(32) Juarez-Perez, E. J.; Wüßler, M.; Fabregat-Santiago, F.; Lakus-Wollny, K.; Mankel, E.; Mayer, T.; Jaegermann, W.; Mora-Sero, I. Role of the Selective Contacts in the Performance of Lead Halide Perovskite Solar Cells. *J. Phys. Chem. Lett.* **2014**, *5*, 680–685.

(33) Guerrero, A.; Juarez-Perez, E. J.; Bisquert, J.; Mora-Sero, I.; Garcia-Belmonte, G. Electrical field profile and doping in planar lead halide perovskite solar cells. *Appl. Phys. Lett.* **2014**, *105*, 133902.

(34) Almora, O.; Guerrero, A.; Garcia-Belmonte, G. Ionic charging by local imbalance at interfaces in hybrid lead halide perovskites. *Appl. Phys. Lett.* **2016**, *108*, 043903.

(35) Bisquert, J.; Bertoluzzi, L.; Mora-Sero, I.; Garcia-Belmonte, G. Theory of Impedance and Capacitance Spectroscopy of Solar Cells with Dielectric Relaxation, Drift-Diffusion Transport, and Recombination. *J. Phys. Chem. C* **2014**, *118*, 18983–18991.

(36) Pockett, A.; Eperon, G. E.; Peltola, T.; Snaith, H. J.; Walker, A. B.; Peter, L. M.; Cameron, P. J. Characterization of planar lead halide perovskite solar cells by impedance spectroscopy, open circuit photovoltage decay and intensity-modulated photovoltage/photocurrent spectroscopy. *J. Phys. Chem. C* **2015**, *119*, 3456–3465.

(37) Beilsten-Edmands, J.; Eperon, G. E.; Johnson, R. D.; Snaith, H. J.; Radaelli, P. G. Non-ferroelectric nature of the conductance hysteresis in $\text{CH}_3\text{NH}_3\text{PbI}_3$ perovskite-based photovoltaic devices. *Appl. Phys. Lett.* **2015**, *106*, 173502.

(38) Kim, H.-S.; Mora-Sero, I.; Gonzalez-Pedro, V.; Fabregat-Santiago, F.; Juarez-Perez, E. J.; Park, N.-G.; Bisquert, J. Mechanism of carrier accumulation in perovskite thin-absorber solar cells. *Nat. Commun.* **2013**, *4*, 2242.

(39) Mora-Seró, I.; Bisquert, J.; Fabregat-Santiago, F.; Garcia-Belmonte, G.; Zoppi, G.; Durose, K.; Proskuryakov, Y. Y.; Oja, I.; Belaidi, A.; Dittrich, T.; Tena-Zaera, R.; Katty, A.; Lévy-Clement, C.; Barrioz, V.; Irvine, S. J. C. Implications of the negative capacitance observed at forward bias in nanocomposite and polycrystalline solar cells. *Nano Lett.* **2006**, *6*, 640–650.

(40) Bisquert, J.; Garcia-Belmonte, G.; Pitarch, A.; Bolink, H. Negative capacitance caused by electron injection through interfacial states in organic light-emitting diodes. *Chem. Phys. Lett.* **2006**, *422*, 184–191.

(41) Itagaki, M.; Taya, A.; Watanabe, K.; Noda, K. Deviations of Capacitive and Inductive Loops in the Electrochemical Impedance of a Dissolving Iron Electrode. *Anal. Sci.* **2002**, *18*, 641–644.

(42) Zhuang, Q.; Xu, J.; Fan, X.; Wei, G.; Dong, Q.; Jiang, Y.; Huang, L.; Sun, S. LiCoO_2 electrode/electrolyte interface of Li-ion batteries investigated by electrochemical impedance spectroscopy. *Sci. China, Ser. B: Chem.* **2007**, *50*, 776–783.

(43) Radvanyi, E.; Van Havenbergh, K.; Porcher, W.; Jouanneau, S.; Bridel, J.-S.; Put, S.; Franger, S. Study and modeling of the Solid

Electrolyte Interphase behavior on nano-silicon anodes by Electrochemical Impedance Spectroscopy. *Electrochim. Acta* **2014**, *137*, 751–757.

(44) Majhi, K.; Bertoluzzi, L.; Keller, D. A.; Barad, H.-N.; Ginsburg, A.; Anderson, A. Y.; Vidal, R.; Lopez-Varo, P.; Mora-Sero, I.; Bisquert, J.; Zaban, A. Co₃O₄-based all-oxide PV: A numerical simulation analyzed combinatorial material science study. *J. Phys. Chem. C* **2016**, DOI: [10.1021/acs.jpcc.6b01164](https://doi.org/10.1021/acs.jpcc.6b01164).

(45) Mosconi, E.; Ronca, E.; De Angelis, F. First-principles investigation of the TiO₂/Organohalide perovskites interface: The role of interfacial chlorine. *J. Phys. Chem. Lett.* **2014**, *5*, 2619–2625.